Performance Estimation of Resonance-Enhanced Dual-Buoy Wave Energy Converter Using Coupled Time-Domain Simulation

Chungkuk Jin [a], HeonYong Kang [a*], MooHyun Kim [a], and Ilhyoung Cho [b]

[a] Department of Ocean Engineering, Texas A&M University, College Station, TX, USA

[b] Department of Ocean System Engineering, Jeju National University, Jeju, Korea

[*] Corresponding author: 3145 TAMU, College Station, TX 77843, USA, Tel: +1-979-847-8710, E-mail: hykang@tamu.edu.

Abstract

This paper presents the modeling methodology and performance evaluation of the resonance-enhanced dual-buoy WEC (Wave Energy Converter) by HEM (hydrodynamic & electro-magnetic) fully-coupled-dynamics time-domain-simulation program. The numerical results are systematically compared with the authors' 1/6-scale experiment. With a direct-drive linear generator, the WEC consists of dual floating cylinders and a moon-pool between the cylinders, which can utilize three resonance phenomena from moon-pool dynamics as well as heave motions of inner and outer buoys. The contact and friction between the two buoys observed in the experiment are also properly modeled in the time-domain simulation by the Coulomb-friction model. Moon-pool resonance peaks significantly exaggerated in linear potential theory are empirically adjusted through comparisons with measured values. A systematic comparative study between the simulations and experiments with and without PTO (power-take-off) is conducted,

and the relative heave displacements/velocities and power outputs are well matched. Then, parametric studies are carried out with the simulation program to determine optimum generator parameters. The performance with various wave conditions is also assessed.

Keywords: Wave Energy Converter; Hydrodynamic-Electro-Magnetic Coupling; Experiment vs Simulation; Linear generator; Dual-cylinder dynamics; Heave resonance; Moon-pool resonance; Optimum energy extraction; Time-domain fully-coupled simulation.

1. Introduction

For sustainable development of a community with minimal environmental problems such as global warming [1, 2], clean renewable energy needs to be continuously developed to be a competitive resource. In particular, ocean wave energy has a gigantic global power potential of 1-10 TW [3, 4]. Wave energy can be an important energy source especially for various offshore operations and isolated islands. In this regard, various types of wave energy converters (WECs) have been devised to convert such clean renewable energy into electrical energy. The WEC can often be categorized into three types; terminator, attenuator, and point absorber [5]. Among them, the point-absorber type has popularly been adopted with the convenience of design and installation compared to multi-connected terminator or attenuator types. Also, the performance of point absorber can be less sensitive to wave direction when tuning for resonance [6].

The use of resonance motion is regarded as a critical aspect of optimal energy extraction as a point absorber under given wave conditions. While many point absorbers utilize resonance motion to amplify power output, most existing concepts use single-frequency resonance using the adjustment of system mass [7] and stiffness [8]. Several authors also suggested multiple-mass systems with LEG (linear electric generator) to take advantage of multi-resonances [9-11]. As an example, to amplify the power production at multiple natural frequencies, a coaxial two-cylinder system was studied in the frequency domain [12]. In their concept, two natural frequencies of the floating cylinders were employed, and no annular moon-pool was considered, assuming zero gap between the two cylinders while independently moving.

Although reliable simulation is essential for the assessment of dual-body WECs, the simulation capacity of previous studies was often limited by less rigorous multi-body hydrodynamic analyses and the use of linear damping or constant PTO (Power-Take-Off) in the frequency-domain calculation [7, 9, 13-17] and time-domain simulations [11, 18, 19]. In regard to the annular gap and its moon-pool resonance, Mavrakos [20] used ideal-fluid-based numerical or analytical methods. However, when considering moon-pool and multi-body resonances, the ideal-fluid methods substantially overestimate the resonance peaks. Therefore, it is recommended to correlate the simulation to experimental data, as suggested in the previous studies of rectangular or cylindrical moon-pools [21, 22]. In the present study, the exaggerated peaks of moon-pool resonances are empirically adjusted based on the experimental results. Also, we developed a hydrodynamics/electro-magnetics fully-coupled simulation program in the time domain. Both hydrodynamic and electro-magnetic fields are simultaneously solved at each time step to best estimate the PTO performance without introducing any representative constant PTO damping parameter, as frequently used in the previous studies.

In this paper, a resonance-enhanced dual-cylinder (outer buoy and inner buoy) WEC with annular moon-pool is devised, and both time-domain simulations and scaled physical experiments are conducted. In [23], authors focused on the design of the WEC and the details of scaled experiments including frequency-domain linear-potential computation. In this study, we developed fully-coupled time-domain simulations including generator dynamics and nonlinear behaviors so that better and direct time-history comparison can be possible. The simulation and experimental results are then systematically compared with the LEG on and off. The comparison shows good agreements, especially after including contact and friction between the two buoys in the simulation modeled as in the experiment. The direct time-series comparisons between the simulation and experiment in random waves were possible by using the experimentally generated wave time series in the simulation. As a PTO system, a direct-drive LEG was employed [9, 24]. It is illustrated that the dual-cylinder WEC can effectively extract wave energy from a wide range of wave frequencies by employing three different resonance phenomena: those of moon-pool, inner cylinder, and outer cylinder. Using the computer simulation program, performance evaluation is conducted with varying LEG parameters so that higher power can be generated in the given wave condition.

2. Resonance-Enhanced Dual-Buoy WEC and Experimental Setup

The resonance-enhanced dual-cylinder WEC consists of two vertical circular cylinders aligned along an identical axis with different diameter, a hollow moon-pool between the two cylinders, and coil and permanent magnet equipped at inner and outer cylinders, respectively. The schematic view and specifications are presented in Fig. 1 and Table 1 [23]. It is designed to place three different natural frequencies of the inner and outer cylinders' heave motions and moon-pool's surface elevation within the range of a given wave spectrum so as to amplify the power production using all the three resonance phenomena. That amplification concept was proven by experiments at a scale ratio of 1:5.95. The experiment was conducted in a wave tank of 110 m length, 8 m width, and 3.5 m depth, as shown in Fig. 2.

At the design stage, the system dimensions were determined by using approximate analytic forms of the three natural frequencies suggested by Fukuda [25] as:

$$\omega_{ni} = \sqrt{\frac{\rho g A_i}{m_i + m_i^a}} \quad i = 1, 2. \tag{1}$$

$$\omega_{nf} = \sqrt{\frac{g}{d_2 + 0.41\sqrt{A_f}}} \tag{2}$$

where ρ represents the density of water, g is gravity acceleration, A_i is the waterplane area of a i th cylinder, m_i and m_i^a are mass and added mass of the i th cylinder, and A_f denotes the waterplane area of the moon-pool. The three natural frequencies of the inner and outer cylinders and moon-pool were set at 3.41 and 3.84 (with added mass of inner and outer cylinders = 0.21 kg and 2.06 kg) and 3.09 rad/sec, respectively [23]. Note that those added masses include hydrodynamic interactions between the two buoys and moon-pool. The same eigenvalues can also be obtained from the corresponding modal analysis of coupled equation of motion. The eigenvalue 3.41 is for the eigenmode of dominant inner buoy motion and negligible outer buoy motion, and 3.84 is for the second eigenmode of negligible inner buoy motion and dominant outer buoy motion. As listed in
Table 2, the experiments include a series of tests with a set of regular waves and one random waves.

There are essential aspects to model the dual-buoy WEC in the time-domain simulation. The model dimensions were used in the time-domain simulation for direct comparison. In the experiments, 4 slack soft springs (stiffness=1.03 N/m) were used to prevent horizontal mean drift motion. These soft springs have a negligible influence on the entire dynamics of two cylinders and corresponding power outputs. In this regard, it was not considered in the time-domain simulations. Moreover, the vertical guide shafts can additionally impose friction force at the contact.

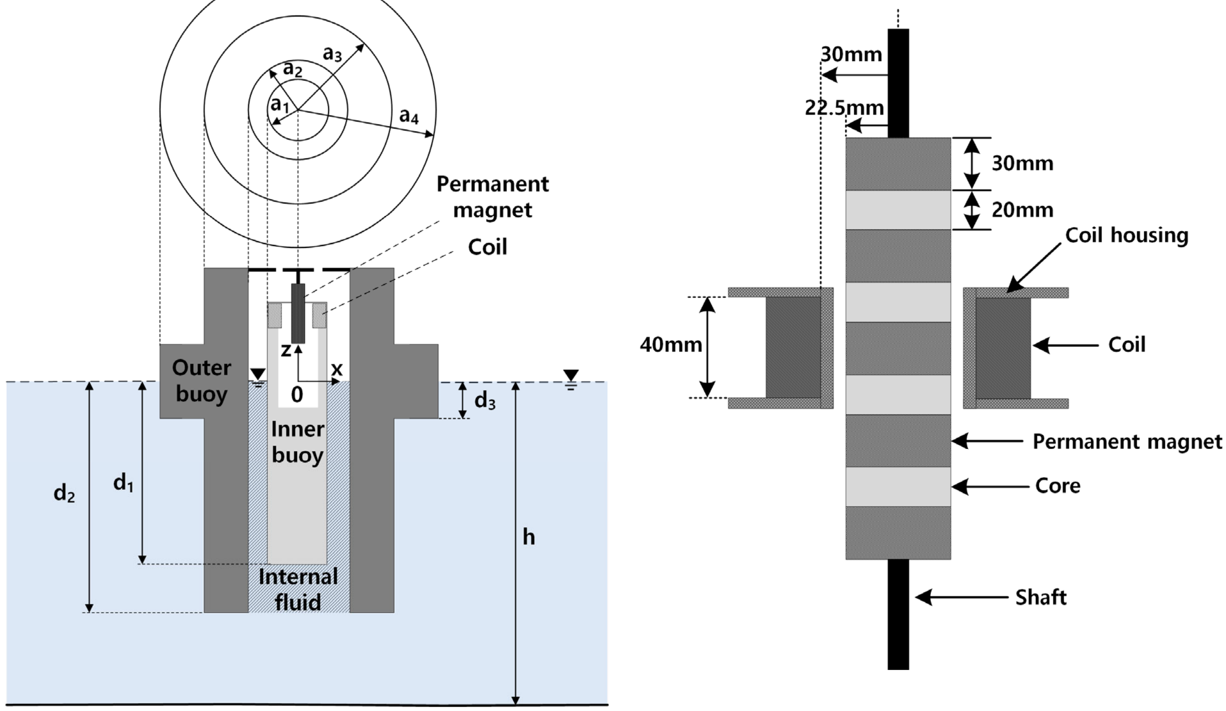

(a) (b)

Fig. 1. Schematic views of two-body WEC system: entire shape (a) and linear generator (b) [23].

Table 1. Dimension of two-body WEC system.

Item	Radius (mm)	Draft (mm)	Height (mm)	Center of gravity (from MWL) (mm)	Mass (kg)
Internal buoy	60 (a_1)	835 (d_1)	1090	-465	9.40
External buoy	95 (a_2)	1000 (d_2)	1500	-500	32.6
	135 (a_3)	168 (d_3)			
	160 (a_4)				

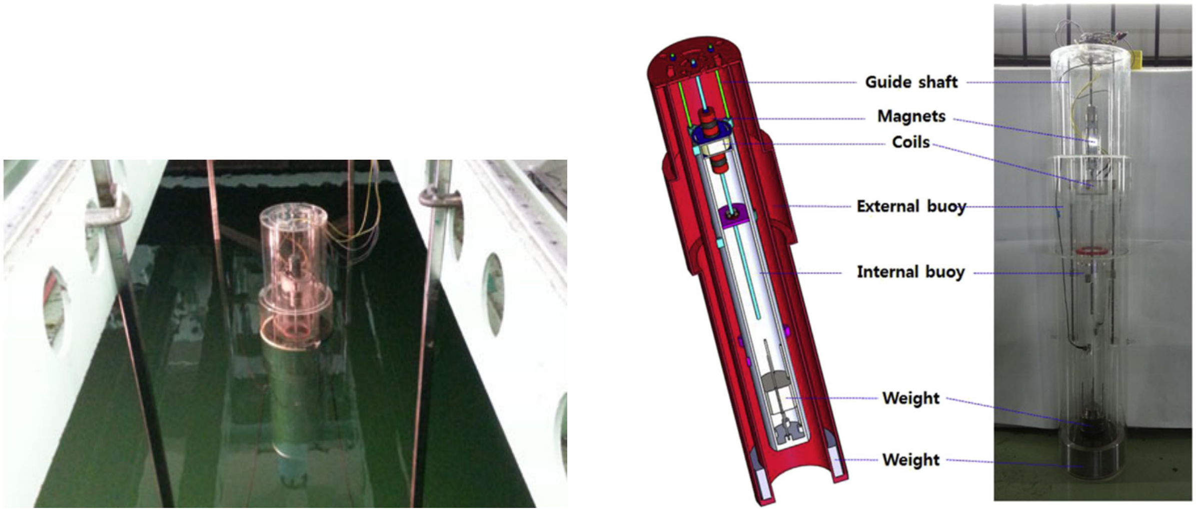

(a) (b)

Fig. 2. Experimental setup in wave tank (a) and WEC model (b) [23].

Table 2 Regular and irregular wave conditions for experiments.

Regular wave							
Case number	Frequency (rad/sec)	Amplitude (m)	Wave steepness	Case number	Frequency (rad/sec)	Amplitude (m)	Wave steepness
1	2.5	0.049	0.01	9	3.5	0.025	0.01
2	2.8	0.039	0.01	10	3.6	0.024	0.01
3	2.9	0.037	0.01	11	3.7	0.023	0.01
4	3.0	0.034	0.01	12	3.8	0.021	0.01
5	3.1	0.032	0.01	13	3.9	0.020	0.01
6	3.2	0.030	0.01	14	4.0	0.019	0.01
7	3.3	0.028	0.01	15	4.1	0.018	0.01
8	3.4	0.027	0.01	16	4.2	0.017	0.01
Irregular wave (JONSWAP spectrum)							
Case number	Peak frequency (rad/sec)	Significant wave height (m)	Gamma				
1	0.074	2.167	3.3				

3. Coupled Time-Domain Simulation for Resonance-Enhanced Dual-Buoy WEC

To accurately assess the performance of the resonance-enhanced dual-cylinder WEC, the dual floating cylinders interacting with each other and a moon-pool should be modeled. In addition, their coupling with the linear generator dynamics needs to be solved simultaneously at each time step. The dynamics of two cylinders in random waves with the PTO turned on can be written in the time domain as an extended form of Cummins' equation [26-28] as follows:

$$(m_{ij}+\Delta m_{ij}^{\infty})\ddot{x}_j + c_{ij}\dot{x}_j + k_{ij}^{T}x_j = f_i^{(1)}(t) + f_i^{C}(t) + f_i^{D}(\mathrm{t}) + f_i^{P}(\mathrm{t}) + f_i^{F}(\mathrm{t}). \quad i,j=1,\ldots,12 \qquad (3)$$

where m_{ij} is the mass matrix, Δm_{ij}^{∞} is the added mass matrix at the infinite frequency, k_{ij}^{T} is the total stiffness matrix, which combines hydrostatic and gravitational restoring stiffness k_{ij}^{H} with any external linear restoring k_{ij}^{E}, and x_j is the displacement. Overdot represents the time derivative of a variable. c_{ij} can be used to represent linear damping mechanism such as mechanical dashpots. $f_i^{(1)}$, f_i^{C}, f_i^{D}, f_i^{P}, and f_i^{F} denote the first-order wave loads, convolution-integral forces related to radiation damping, Morison-formula-based viscous damping loads, generator's reaction forces known as power-take-off (PTO) damping, and friction loads induced by the contact of vertical shafts, respectively. The first 6 subscripts are 6 DoFs of the inner cylinder, and the second 6 subscripts are those of the outer cylinder.

Assuming Gaussian linear random waves, describable by the superposition of regular wave components, Δm_{ij}^{∞}, f_i^{C}, and $f_i^{(1)}$ are obtained by Fourier Transform between impulse-response-function-based dynamic equation in the time domain and linear-diffraction/radiation-based dynamic equation in the frequency domain as:

$$\Delta m_{ij}^{\infty} = \Delta m_{ij}(\omega_{\max}) + \int_0^{\infty} r_{ij}(t)\frac{\sin(\omega_{\max} t)}{\omega_{\max}} dt. \tag{4}$$

$$f_i^C(t) = -\int_0^{\infty} r_{ij}(\tau)\dot{x}_j(t-\tau)d\tau. \tag{5}$$

$$r_{ij}(t) = \frac{2}{\pi}\int_0^{\infty} b_{ij}(\omega)\cos(\omega t)d\omega. \tag{6}$$

$$f_i^{(1)}(t) = \mathrm{Re}\left(\sum_{j=1}^{N} A_j d_l(\omega_j) e^{i(k_j x - \omega_j t - \alpha_j)}\right). \tag{7}$$

where $\Delta m_{ij}(\omega_{\max})$, $b_{ij}(\omega)$, and $d_l(\omega_j)$ are added inertia, radiation damping, and linear wave excitation at the respective frequencies, and they can be calculated from the three-dimensional linear diffraction/radiation of the two cylinders, and A_j, k_j, ω_j, and α_j are, respectively, wave amplitude, wavenumber, wave frequency, and random-phase angle. As the two cylinders are modeled by two sets of panel discretization with the annular moon-pool between them, those hydrodynamic coefficients represent their interactions with the moon-pool. As shown in Fig. 3, we used 1636 panels for the inner cylinder and 5252 panels for the outer hollow cylinder. To maintain numerical accuracy, the panel size of two cylinders is smaller than 2/3 of the gap distance. The convergence with the panel numbers was checked. Taking the experiment scale, the hydrodynamic coefficients were computed for 50 wave frequencies from 1.5 to 9.0 rad/s.

The moon-pool resonance results in the rapid change and overestimated peaks of $\Delta m_{ij}(\omega_{\max})$, $b_{ij}(\omega)$, and $d_l(\omega_j)$ near the lowest (Helmholtz mode) moon-pool resonance frequency when they are calculated from the ideal-fluid-based diffraction/radiation program. In reality, the peaks are limited by viscous and nonlinear effects. The exaggerated peaks can be adjusted empirically by comparison with experimental values such that motion-response peaks match at the respective resonance frequencies [29]. We selected such a correlation method by taking advantage of the experimental data. Alternative CFD simulations based on the Navier-Stokes equation also require verifications with experimental data while the computation is substantially more complex and time-consuming. Furthermore, its coupling with the given WEC's PTO may not be straightforward.

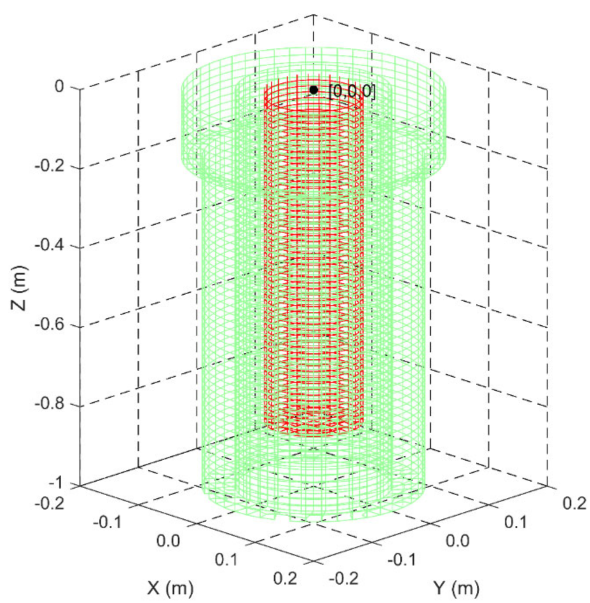

Fig. 3. Panel models of the two cylinders.

As shown in Fig. 2b, there are two (front and rear) vertical shafts with protruded guides to narrow the gap between the inner and outer buoys. Those guides create synchronous surge/sway and pitch/roll motions between the two buoys while allowing relative heave motions, which was also observed in the experiment. The guides were employed to maintain the constant gap between the magnet and coil in the PTO system. Friction forces occur due to the protruded guides between the two buoys with time-varying contact forces. The time-varying contact forces can numerically be modeled by linear horizontal springs at the locations of the guides. We employed a total of 12 highly stiff horizontal springs at the top, middle, and bottom locations of the inner cylinder at four sides along x and y axes between the two buoys, k_x and k_y, and a highly stiff angular spring in yaw, k_ψ. The stiffness was determined to warrant the synchronous surge/sway and pitch/roll motions between the two buoys, as shown below as 12 by 12 stiffness matrix, where h_x and h_y represent the moment arm from the origin located at mean water level:

$$
\begin{array}{llll}
k_{1,1}^E = \sum k_x, & k_{1,5}^E = \sum k_x h_x, & k_{1,7}^E = -\sum k_x, & k_{1,11}^E = -\sum k_x h_x, \\
k_{2,2}^E = \sum k_y, & k_{2,4}^E = -\sum k_y h_y, & k_{2,8}^E = -\sum k_y, & k_{2,10}^E = \sum k_y h_y, \\
k_{4,4}^E = \sum k_y h_y^2, & k_{4,8}^E = \sum k_y h_y, & k_{4,10}^E = -\sum k_y h_y^2, & k_{5,5}^E = \sum k_x h_x^2, \\
k_{5,7}^E = -\sum k_x h_x, & k_{5,11}^E = -\sum k_x h_x^2, & k_{6,6}^E = \sum k_\psi, & k_{6,12}^E = -\sum k_\psi, \\
k_{7,7}^E = \sum k_x, & k_{7,11}^E = \sum k_x h_x, & k_{8,8}^E = \sum k_y, & k_{8,10}^E = -\sum k_y h_y, \\
k_{10,10}^E = \sum k_y h_y^2, & k_{11,11}^E = \sum k_x h_x^2, & k_{12,12}^E = \sum k_\psi. &
\end{array}
\tag{8}
$$

As a symmetric matrix, we applied k_{ij}^E, as given in Table 3. The stiffness values in the table were selected to warrant the synchronous pitch/surge motions between the two buoys. We further checked the higher spring stiffness than the selected values and the contact-force results were not sensitive to the variation.

Table 3. External stiffness matrix for guide-shaft modeling.

Stiffness coefficient	Stiffness	Stiffness coefficient	Stiffness	Stiffness coefficient	Stiffness
$k_{1,1}^{E}$	1.8×10^{7}	$k_{4,4}^{E}$	5.1×10^{6}	$k_{7,7}^{E}$	1.8×10^{7}
$k_{1,5}^{E}$	-5.2×10^{6}	$k_{4,8}^{E}$	-5.2×10^{6}	$k_{7,11}^{E}$	-5.2×10^{6}
$k_{1,7}^{E}$	-1.8×10^{7}	$k_{4,10}^{E}$	-5.1×10^{6}	$k_{8,8}^{E}$	1.8×10^{7}
$k_{1,11}^{E}$	5.2×10^{6}	$k_{5,5}^{E}$	5.1×10^{6}	$k_{8,10}^{E}$	5.2×10^{6}
$k_{2,2}^{E}$	1.8×10^{7}	$k_{5,7}^{E}$	5.2×10^{6}	$k_{10,10}^{E}$	5.1×10^{6}
$k_{2,4}^{E}$	5.2×10^{6}	$k_{5,11}^{E}$	-5.1×10^{6}	$k_{11,11}^{E}$	5.1×10^{6}
$k_{2,8}^{E}$	-1.8×10^{7}	$k_{6,6}^{E}$	7.5×10^{7}	$k_{12,12}^{E}$	7.5×10^{7}
$k_{2,10}^{E}$	-5.2×10^{6}	$k_{6,12}^{E}$	-7.5×10^{7}		

The friction force, f_i^F, induced by the contacts at the protruded guides of the vertical shafts, can be given by Coulomb friction

$$f_3^F = \mu N \mathrm{sign}\left(\dot{z}_{rel}\right) \text{ and } f_9^F = -f_3^F \tag{9}$$

where μ is the friction coefficient, N is normal contact force, and $\dot{z}_{rel}$ are heave velocity of the outer cylinder relative to the inner cylinder. The opposite heave relative motion with the contact results in resisting friction force to both cylinders in the heave direction. The contact forces can be different at the top, middle, and bottom springs due to the relative surge and pitch motions with contact. For head sea condition, N results from all the restoring loads in the surge direction as:

$$\begin{aligned} N_3 &= \left|k_{1j}^T x_j\right| = \left|k_{1,1}x_1 + k_{1,5}x_5 + k_{1,7}x_7 + k_{1,11}x_{11}\right|, \\ N_9 &= \left|k_{7j}^T x_j\right| = \left|k_{7,1}x_1 + k_{7,5}x_5 + k_{7,7}x_7 + k_{7,11}x_{11}\right|. \end{aligned} \tag{10}$$

To include additional energy dissipation in heave by water viscosity, viscous damping coefficients in heave direction, c_{33}=1.6 kg/s and c_{99}=9.1 kg/s for inner and outer cylinders, were obtained from the free-decay test in the experiment without friction. In this regard, no additional Morison members were employed in the heave direction, i.e., $f_i^D = 0$.

For power generation, the direct-driven LEG (linear electrical generator) is used. It results in the power-take-off damping loads f_i^P induced by Electromotive Force (EMF), which generates the electrical current to restore constant magnetic flux density during the relative motion between the magnet and coil. According to Faraday's law of induction, EMF can be expressed as [7, 10, 30]:

$$E = \frac{d\lambda_{fl}}{dt} = \frac{dz_{rel}}{dt}\frac{d\lambda_{fl}}{dz_{rel}} = \dot{z}_{rel}\frac{d\lambda_{fl}}{dz_{rel}} \tag{11}$$

where $\lambda_{fl}\left(= N_c\phi_m\right)$ is flux linkage given by the number of turns N_c and magnetic flux ϕ_m. z_{rel} is heave displacement of the outer cylinder (permanent magnet) relative to the inner cylinder (coil). The induced current, i, is obtained by solving a resistor-inductor (RL) circuit, which consists of EMF, phase-inductance (L_C), phase-resistance (R_C), and load-resistance (R_L) as:

$$E = \left(R_L + R_C\right)\cdot i + L_C\frac{di}{dt}, \tag{12}$$

f_i^P can be calculated by the Lorentz-force equation. For the inner cylinder,

$$f_3^P(t) = i\oint d\vec{l} \times \vec{B} = -B_m l i \quad \text{and} \quad f_9^P(t) = -f_3^P(t) \tag{13}$$

where l and B_m ($= B_f \cos(\pi / \tau z)$ with the magnitude of magnetic flux density, B_f) are total length of coil and the magnetic flux density. Although $\vec{B}$ can be found from a finite element analysis of the magnet flux, we obtained the value by comparing the simulation with the experiment. Equal and opposite directional force acts on the outer cylinder following the opposite relative motion. Consequently, the generated power output is

$$P_{out} = i^2 R_L = i V_o \tag{14}$$

where V_o is the output voltage.

Fig. 4 presents a schematic view, explaining the coupling between the dynamics of the two floating bodies in random waves in Eq. (3), and the dynamics of the linear generator in Eqs. (11) to (14). Generator dynamics generate higher-frequency outputs compared with the floating body's dynamics. In that regard, 1/50 time interval (0.0002 seconds) of the floating bodies' dynamics was chosen for generator dynamics, which means that for every 50-time steps of computing Eqs. (11) to (14), the motions of Eq. (3) are solved with the renewed f_i^P.

Moreover, while solving Eq. (3) for x_j at n+1 time step in integral formation, f_i^P at n+1 time step is obtained by Adams-Bashforth explicit scheme due to the unknown values at n+1 time step, which is consistent with the other right-hand-side terms of Eq. (3).

$$\int_{t(n)}^{t(n+1)} f_i^P dt = \frac{\Delta t}{2}\left(3 f_i^{P(n)} - f_i^{P(n-1)}\right) \tag{15}$$

Physically, it represents the energy consumed to generate the electrical power for the 50 steps of the generator dynamics, which is otherwise one single step of the floating bodies' dynamics.

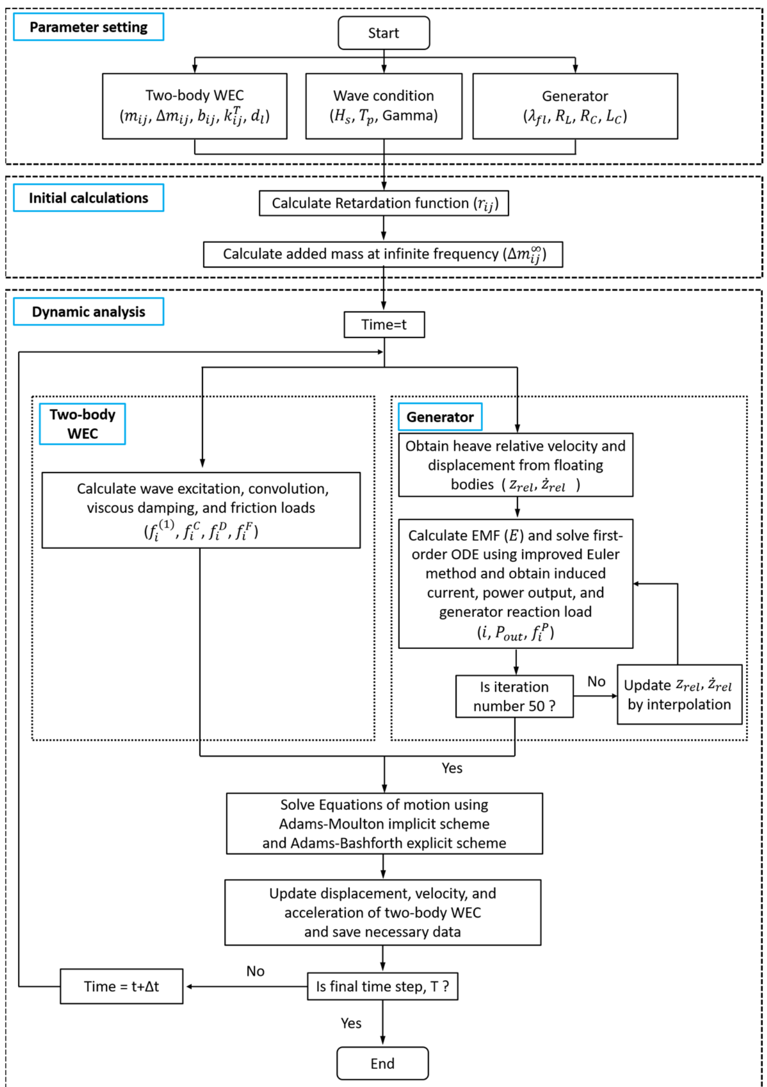

Fig. 4. Schematic view of coupling the generator dynamics with floating body dynamics.

To solve Eq. (16), we used the improved Euler method. As the LEG parameters used in the experiment, we adopted load and phase resistances of 200 and 11.74 Ω, respectively, while phase inductance is 0.0596 H. After the validation of this coupled time-domain simulation against the experimental measurement, we conducted sensitivity studies with varying LEG parameters to find the optimal performance of the respective PTOs for a given random sea state.

4. Results and Discussions

4.1. Comparisons of Numerical Simulations with Experimental Data

Using the three-dimensional potential-flow-based radiation/diffraction panel program, we obtained hydrodynamic and hydrostatic coefficients of the two-body system. The interactions of the two bodies with the moon-pool and incoming waves are presented by 12-by-12 matrices of added inertia and radiation damping. The incident wave excitations are given for the respective 6 DoFs of each body.

Before solving the coupled dynamics of the dual buoys with PTO, we first confirmed the numerical modeling of the employed LEG and the numerical power calculation scheme as described in the previous section. In this regard, we inputted the measured relative heave displacement/velocity data corresponding to the measured power output in the numerical LEG simulation. Fig. 5 shows well-matched power outputs between the physical and numerical models as the relative displacement and velocity are identical. Judging from the EMF formula, note that the power output magnitude is strongly dependent on the relative velocity while the signal tendency is related to the relative displacement.

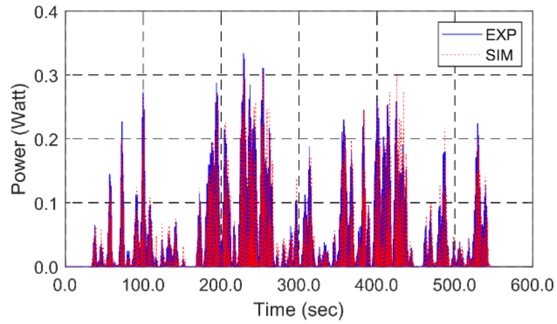

Fig. 5. Confirmation of numerical power calculation scheme.

Next, let us consider the hydrodynamic interactions of the dual buoys with and without the LEG. When we want to directly compare the time series of motions and power outputs between the physical and numerical models, it is important to use the experimental incident-wave time series in the corresponding numerical simulation. From the time series of wave elevation measured in the experiment, we performed Fast Fourier Transform (FFT) to obtain magnitudes and phases of the wave components and recovered the exactly same time series and spectra of the wave elevation in the simulation by superposing 655 regular wave components as confirmed in Fig. 6.

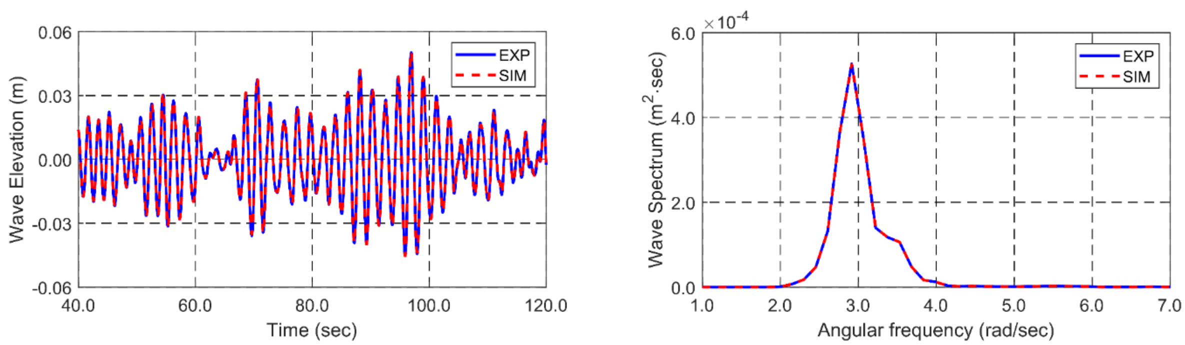

(a) (b)

Fig. 6. Time series of wave elevation (b) and corresponding spectra (b).

In the dynamics of the two floating bodies, we first confirmed whether the 5 DoFs except for the heave are synchronized, as observed in the experiment with the applied set up, between the two bodies when using the applied 12-by-12 stiffness matrix. Fig. 7 demonstrates that the condition is well realized in the present numerical simulation with respect to the surge and pitch motions. It is already explained that the synchronous surge and pitch motions are due to the narrow gap between the two buoys by using protruded guides allowing only heave relative motions, which is now well realized in the numerical-simulation program.

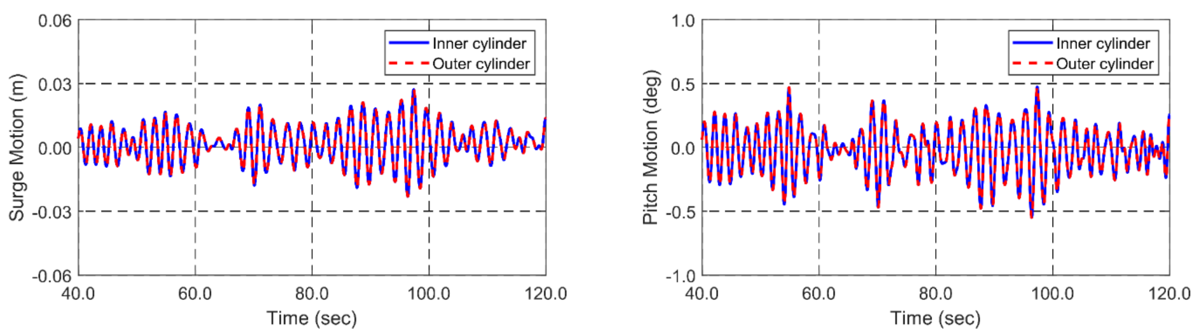

(a) (b)

Fig. 7. Synchronized motions between the two buoys: (a) surge motion, (b) pitch motion.

Next, let us consider the hydrodynamic performance of the dual buoys without the linear generator. For a good comparison between the numerical and experimental results, the moon-pool and motion resonances and friction forces at the contacts need to be reasonably modeled. In the present case, the heave resonance frequency of the inner buoy is close to that of the lowest moon-pool resonance. Potential theory tends to significantly exaggerate the peak amplitude and its rapid variation in the hydrodynamic coefficients near the moon-pool resonance.

To reduce the unphysical overestimation, we empirically adjusted the exaggerated peak behaviors at the moon-pool resonance frequency, 3.15 rad/sec, to be more reasonable, as shown in Fig.8. The similar trends can also be obtained by placing an artificial moveable lid with damping on the free-surface of the annular moon-pool [29]. The empirical adjustments can be validated by good comparisons of peaks between numerical and measured motions near the frequency.

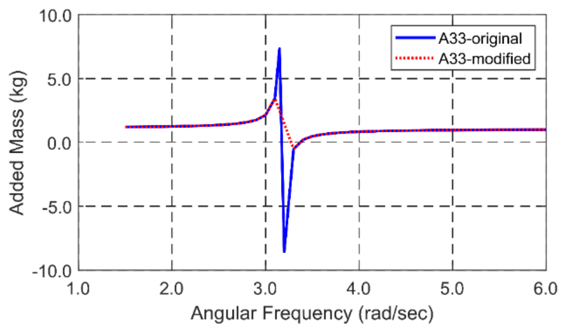

(a) Added mass (inner cylinder)

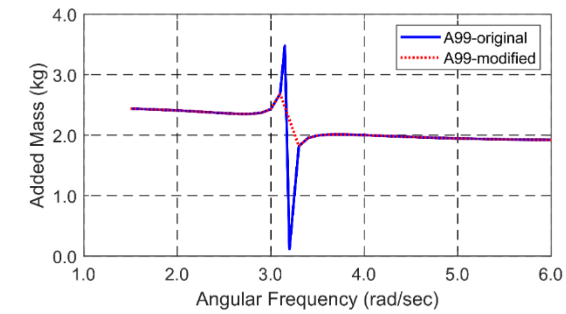

(b) Added mass (outer cylinder)

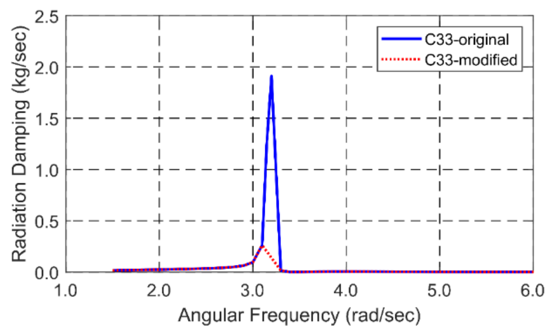

(c) Radiation damping (inner cylinder)

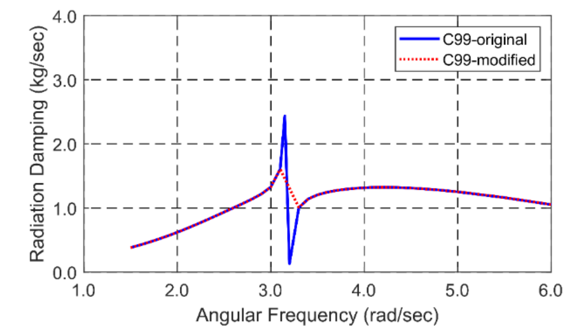

(c) Radiation damping (outer cylinder)

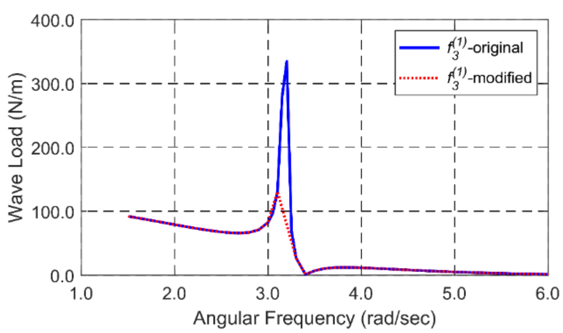

(e) Wave load per unit amplitude
(inner cylinder)

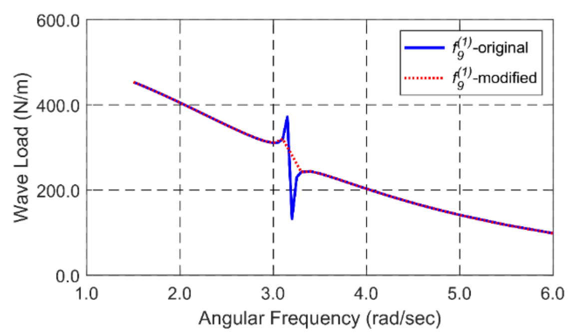

(f) Wave load per unit amplitude
(outer cylinder)

Fig. 8. Potential-theory-based hydrodynamic coefficients in heave with the peak empirically adjusted: added mass, radiation damping, and first-order wave load.

Fig. 9 shows the heave RAOs for the inner and outer buoys without power generation. When the original potential theory is used by using the frequency-domain multi-body linear diffraction/radiation program, the heave-resonance peak of the inner buoy is significantly overestimated due to the exaggerated moon-pool behavior. The lowest up-and-down pumping mode of the moon-pool fluid motions further stimulates the inner-buoy resonant motions. However, in reality, the moon-pool fluid motions are limited by viscosity and nonlinearity, which results in a smaller peak compared to the potential theory, as observed in the experiment. On the other hand, the second minor peak near 3.6 rad/s is significantly underestimated by the linear potential theory when compared to the experimental value. The heave resonance of the outer buoy is also overestimated by the potential theory but its degree is milder since outer-buoy heave resonance frequency is away from the moon-pool resonance frequency. Since the potential-theory-based 3D multi-body diffraction/radiation program does not reasonably predict the heave relative motions of the dual-buoy system, we employed the present time-domain simulation program based on Eq. (3) so that it can represent the physics of the experimental set-up as close as possible, including the moderated moon-pool motions and mechanical friction forces between the two buoys. As a result, we can observe much better agreement between the simulation and experimental results. The time-domain RAO (blue solid line) was constructed by a single time-domain simulation using the random wave of Fig. 6 from the square-root of the heave spectrum divided by wave spectrum. In the time-domain simulation, to include the effect of the friction force by the vertical shafts, we applied f_i^F with the friction coefficient, 0.28. After f_i^F is applied, the second minor peak of the inner-buoy heave near 3.6 rad/s is recovered as observed in the experiment. It is the result of frictional interaction between the inner and outer buoys. When the friction force is removed in the time-domain simulation program, the second minor peak disappears. Fig. 10 shows the time series of the incident wave elevation and relative heave motion. It clearly demonstrates that the relative heave motions are well amplified compared to the incident wave amplitudes.

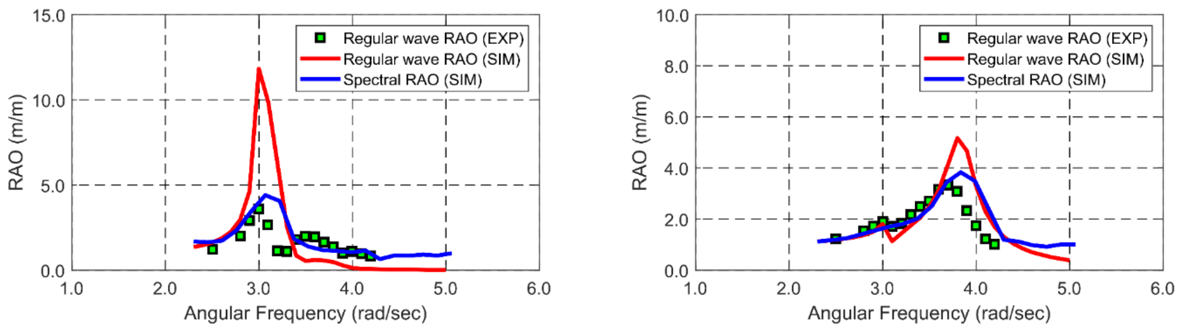

(a) (b)

Fig. 9. Heave RAOs without a linear generator: (a) inner cylinder, (b) outer cylinder (Regular wave RAO (EXP) = RAO from regular wave tests; regular wave RAO (SIM) = RAO from frequency-domain potential theory; Spectral RAO (SIM) = RAO obtained from response and wave spectra in random waves by time-domain simulation).

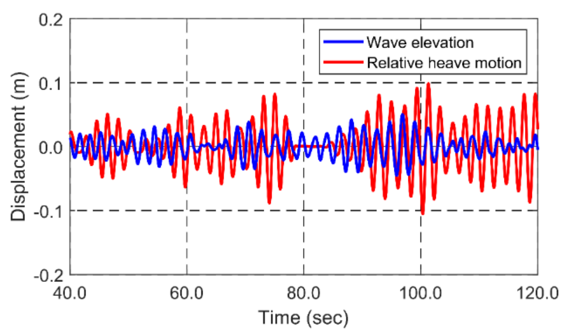

Fig. 10. Comparison between incident wave elevation and relative heave motion.

Since the hydrodynamic performance of the dual-buoy WEC is well validated, we next consider the case with LEG turned on, i.e., full hydrodynamic and electro-magnetic coupled dynamics of the given system. The present time-domain numerical simulation results for the random waves are compared with both regular- and irregular-wave experimental results in Fig. 11. The regular and irregular wave tests produced almost the same results, as a double-checking of the model test. Fig. 11 shows that the motion peaks of inner and outer buoys are reduced compared to Fig. 9 when the LEG is turned on. The same trend can be observed in the numerical simulations. The general trend of the physical test and time-domain simulation is well matched. The second minor peak of the inner-buoy heave near 3.5 rad/s is more pronounced with the enhanced interaction between inner and outer buoys with additional electro-magnetic force at the LEG, which is well reproduced in the present hydrodynamic and electro-magnetic coupled dynamic simulation.

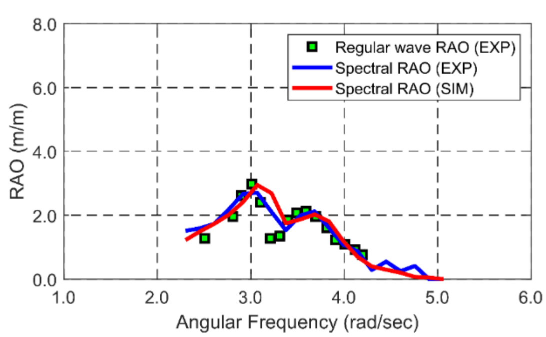

(a)

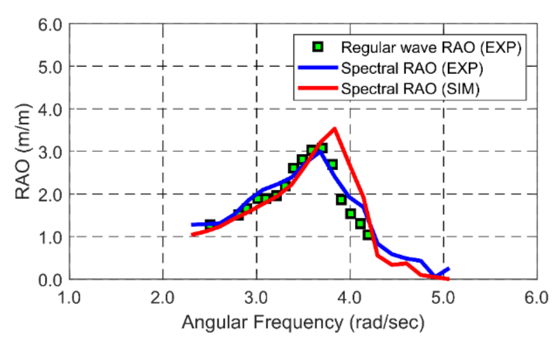

(b)

Fig. 11. Heave RAOs with a linear generator connected: (a) inner cylinder, (b) outer cylinder (Spectral RAO (EXP) = spectral RAO obtained by FFT of heave motions induced by random waves from the experiment).

Figs. 12-13 show the time histories and spectra of the relative heave displacement and velocity obtained from model test and numerical simulation with the LEG turned on. We can observe very good agreement between them, which demonstrates that the present fully-coupled time-domain simulation program well represents the physical WEC system.

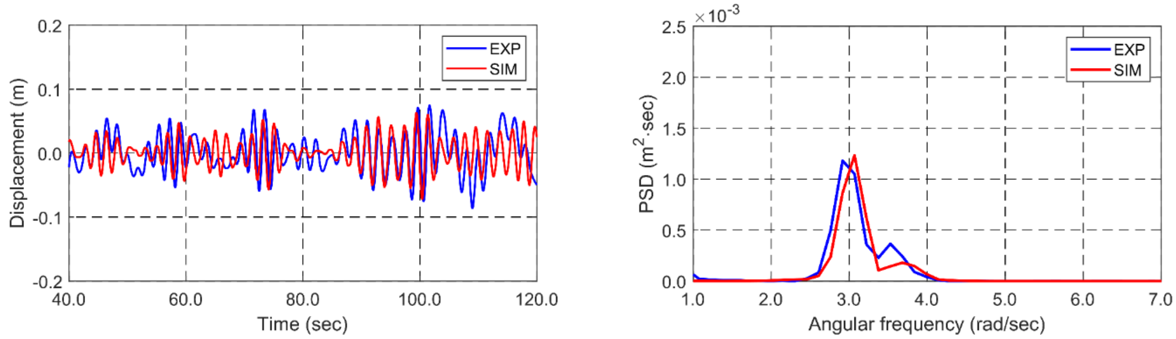

(a) (b)

Fig. 12. Comparison of time histories (a) and spectra (b) of relative heave displacements.

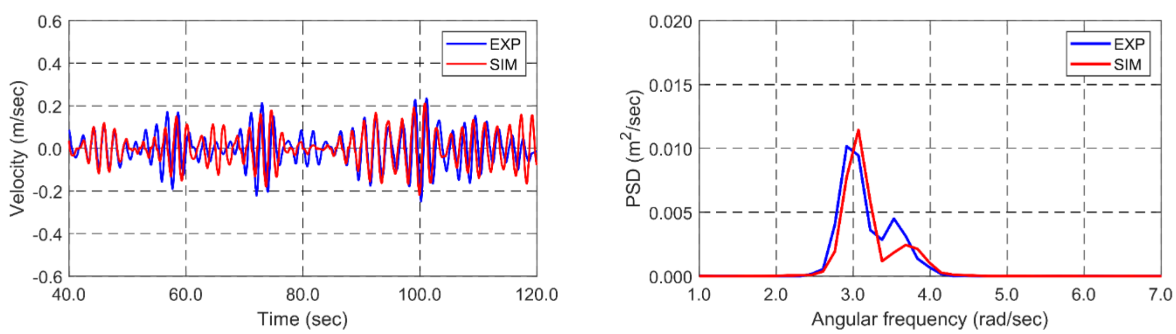

(a) (b)

Fig. 13. Comparison of time histories (a) and spectra (b) of relative heave velocities.

Next, the measured and simulated time series and spectra of the power outputs are given in Fig. 14. The agreements of the magnitudes and tendencies in time series and the corresponding spectra are well matched, which confirms that the developed hydrodynamic and electro-magnetic fully-coupled dynamics program is valid. The average power output from the time-domain simulation is 0.0154 Watt, which is very close to the experimental value. The small discrepancy in the time-series comparison comes from the minor differences between the measured and simulated relative heave motions and velocities in Figs. 12 and 13. Since the wave power is mainly proportional to the square of free-surface elevation, the first two peaks are located near the sum and difference frequencies of the input wave spectrum. Statistical data corresponding to Figs. 12-14 are presented in Table 4.

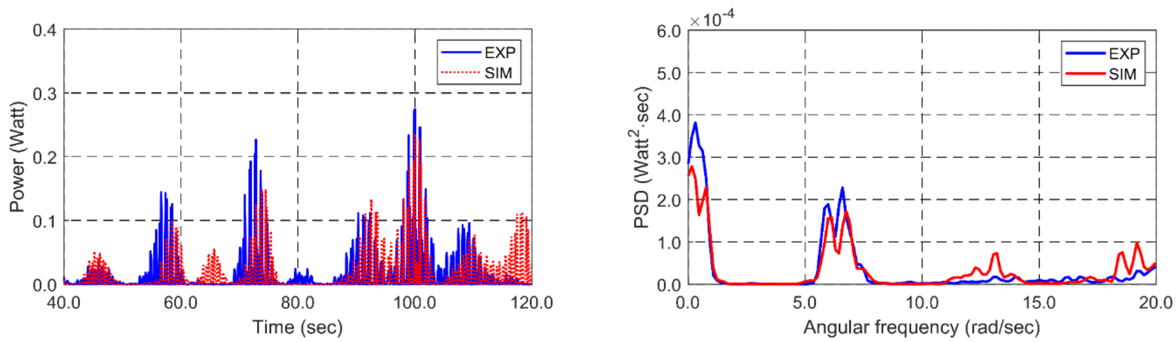

(a) (b)

Fig. 14. Comparison of time histories (a) and spectra (b) of power output.

Table 4. Average, standard deviation, and maximum/minimum values of relative displacement, relative velocity, and power output.

Item	Parameter					
	Relative displacement (m)		Relative velocity (m/s)		Power output (W)	
	EXP	SIM	EXP	SIM	EXP	SIM
Average value	0	0	0	0	0.015	0.015
Standard deviation	0.030	0.027	0.079	0.076	0.030	0.027
Maximum value	0.073	0.065	0.234	0.211	0.270	0.238
Minimum value	-0.085	-0.075	-0.248	-0.220	0	0

4.2. Optimum Performance Estimation

In the previous section, we validated the developed WEC simulation program through comparisons with a series of experimental results. In the comparison, the load resistance (R_L) was fixed to be 200 Ω as the value used in the experiment. However, the variation of the load resistance can be critical to find the optimum performance. For instance, a large value of load resistance may decrease the power output owing to reduced power input by a reduction in induced current, even if efficiency becomes high. On the other hand, a small load resistance results in large induced current, which also leads to a significant generator's reaction load. The massive generator's reaction load can also reduce power generation. Therefore, an optimal power generation can be optimized through the adjustment of load resistance.

Although the impedance matching method is well-known to seek maximum power generation of a single-DOF wave energy converter of constant mass, spring, and damper with harmonic excitation [31], it may not directly be applicable to this resonance-enhanced dual-buoy WEC because the generation results from 12 DOFs interacting each other with random waves involving the corresponding frequency-dependent inertia and damping coefficients. Also, the WEC is designed to utilize three resonances in time-varying random waves, so the selection of optimal generator parameters is not that straightforward. To generate high average power output with variable generator parameters in a typical random wave, we performed parametric study as follows.

The load resistances vary from 20-200 Ω with the 5-Ω interval while keeping the same experimental incident-wave profile as given in Fig. 6. As presented in Fig. 15, the parametric study shows that the optimum load resistance is 130 Ω, and the average power output increases by 4.3 % compared with the initial load resistance of 200 Ω. That optimum load resistance was used in the following simulations. The power output significantly increases with the increase of load resistance until 100 Ω. Afterward, we observed only minor variations. It is also interesting that the load resistances for the maximal power input, proportional to EMF, and output, measured at the load resistance, are different, which means that the load resistance generating the maximum relative heave velocity is not necessarily the optimal value.

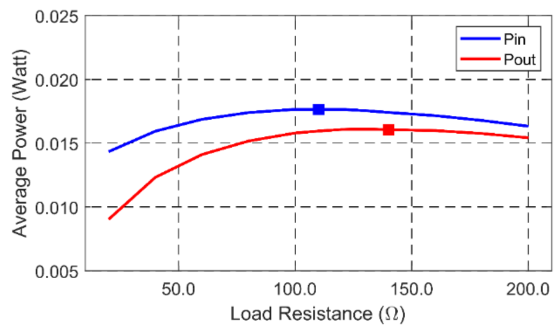

Fig. 15. Average power input and output at different load resistances (square box means the load resistance at the maximum average power).

After the load resistance was optimized, we conducted another parametric study to optimize the magnitude of EMF. In general, larger EMF magnitude can produce higher power. However, larger EMF magnitude induces larger generator's reaction load, resulting in reduced power output. Therefore, there also exists the optimal magnitude of EMF, as shown in Fig. 16. In the figure, the magnitude of magnetic flux density, B_f, was varied from 0.068 to 0.34 T. The optimum magnitude of magnetic flux density is found to be 0.19 T, which is about 1.1 times the initial value of 0.170 T used in the experiment. When the magnitude of magnetic flux density is higher than 0.19 T, the average power output drops due to the increased generator's reaction load.

The optimal magnetic flux of 0.19 T results in power output increases by 0.7 %, which implies that the experimental value of magnetic flux density was already near optimum. When the magnetic flux density is less than 0.15 T, the average power output continues to drop significantly, as shown in Fig. 16.

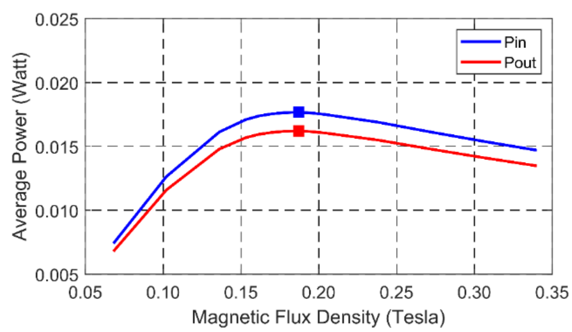

Fig. 16. Average power input and output at different magnitudes of magnetic flux density (square box means the magnitude of the magnetic flux density at the maximum average power).

Through these parametric studies with the given sea state, the optimum parameters for the generator were determined as load resistance of 130 Ω and magnetic flux density of 0.19 T. The performance of the optimum WEC design was checked for different sea states. In this regard, the time histories of wave elevation for various wave conditions were generated using various JONSWAP wave spectra. Significant wave height and enhancement parameter were fixed at 0.168 m and 3.3 while peak period was varied from 1.23 to 3.08 sec as the experimental scale. The same significant wave height means the same area under the wave spectra, i.e., same wave energy. 100 regular wave components were superposed with randomly perturbed central frequencies. The lower and upper cut-off frequencies of the incident wave spectra were set to be 0.7 and 2.2 times of peak frequency. Fig. 17 shows the average power outputs for the two LEG designs (original and optimal) and varying wave conditions. It shows that under the optimal PTO damping condition, average power outputs are 7.8 - 30.6 % larger than the original PTO damping regardless of the change in peak wave frequencies. The increase of mean power output is especially large in the range of 3.4 - 4.0 rad/s. The maximum power output occurs when the peak frequency of the wave spectrum is near the heave natural frequency of the outer buoy, as shown in Fig. 17 for both PTO damping conditions. The bandwidth of high power output is wide by intentionally separating the heave resonance frequencies of inner and outer buoys, as suggested in Cho and Kim [32]. When more rigorous multi-variable optimization is needed, we may use MMA (method of moving asymptotes) to achieve the wide bandwidth of two target modes [33].

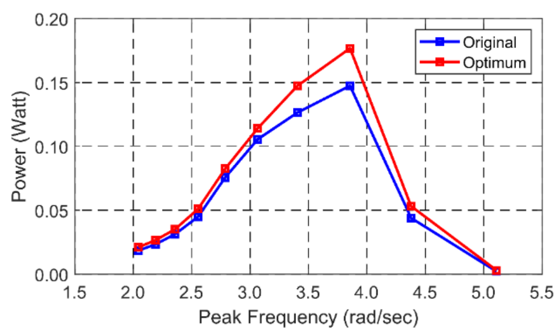

Fig. 17. Average power output under optimum and original PTO conditions.

5. Conclusions

The performance of the resonance-enhanced dual-buoy WEC was estimated through time-domain simulations correlated to the experiments. The proposed WEC was devised to utilize three resonances; heave resonances of dual cylinders and moon-pool resonance to maximize power generation while most point absorbers took advantage of one or two heave natural frequencies. As a result, our WEC has a wider wave-frequency range of high performance.

In the time-domain simulation, floating bodies were fully coupled with a linear generator by a full HEM interaction. Also, friction effects between the vertical shafts and buoys were properly modeled in the time-domain simulation to improve comparisons against model tests. Moon-pool resonance peaks in hydrodynamic coefficients exaggerated by the linear potential theory are empirically moderated to better compare with measured motions. A systematic comparative study between experiments and simulations was performed for a scaled model to validate the developed HEM fully-coupled time-domain simulation program with and without PTO. The simulated relative heave displacements/velocities and generated power outputs were well matched against measured values with and without the LEG. The developed program is to be much more efficient than computationally expensive CFD simulations while producing reliable results compared to experiments. Also, it is hard to find the CFD program coupled with generator dynamics.

The optimum LEG parameters were determined through a series of parametric studies. At the optimized load resistance and magnetic flux density, the average power outputs were increased by 7.8 - 30.6 %. Moreover, high-quality power output was possible in the range of 3 - 4 rad/s by effectively separating the inner and outer buoy resonances. This wide bandwidth of high power output demonstrates that our system worked as purposed. Further improvement of proto-type design can be made by applying the developed time-domain-simulation program.

Acknowledgment

This research is supported by a U.S. DOE EERE WPTO project, DE-EE0008630. This work is also supported by the National Research Foundation of Korea(NRF) grant funded by the Korea government(MSIT) (No. 2017R1A5A1014883).

References

[1] Herzog AV, Lipman TE, Kammen DM. Renewable energy sources. Encyclopedia of Life Support Systems (EOLSS). Forerunner Volume-‘Perspectives and Overview of Life Support Systems and Sustainable Development2001.

[2] Nations U, Transforming our world: The 2030 agenda for sustainable development. General Assembley 70 session, (2015).

[3] López I, Andreu J, Ceballos S, de Alegría IM, Kortabarria I. Review of wave energy technologies and the necessary power-equipment. Renewable and Sustainable Energy Reviews2013. p. 413-434.

[4] Mork G, Barstow S, Kabuth A, Pontes MT. Assessing the global wave energy potential. ASME 2010 29th International conference on ocean, offshore and arctic engineering: American Society of Mechanical Engineers; 2010. p. 447-454.

[5] Dallman A, Jenne DS, Neary V, Driscoll F, Thresher R, Gunawan B, Evaluation of performance metrics for the Wave Energy Prize converters tested at 1/20th scale. Renewable and Sustainable Energy Reviews, 98 (2018) 79-91.

[6] Bull D, Ochs ME, Laird DL, Boren B, Jepsen RA, Technological cost-reduction pathways for point absorber wave energy converters in the marine hydrokinetic environment. Sandia National Laboratories, (2013).

[7] Stelzer M, Joshi R, Evaluation of wave energy generation from buoy heave response based on linear generator concepts. Journal of Renewable and Sustainable Energy, 4 (2012) 063137.

[8] Polinder H, Damen ME, Gardner F, Linear PM generator system for wave energy conversion in the AWS. IEEE transactions on energy conversion, 19 (2004) 583-589.

[9] Gao Y, Shao S, Zou H, Tang M, Xu H, Tian C, A fully floating system for a wave energy converter with direct-driven linear generator. Energy, 95 (2016) 99-109.

[10] Park S-S, Park SM, Jung J, Kim JH, Analysis and experiments of the linear electrical generator in wave energy farm utilizing resonance power buoy system. Journal of Magnetics, 18 (2013) 250-254.

[11] Engström J, Kurupath V, Isberg J, Leijon M, A resonant two body system for a point absorbing wave energy converter with direct-driven linear generator. Journal of applied physics, 110 (2011) 124904.

[12] Wang L, Son D, Yeung RW, Effect of mooring-line stiffness on the performance of a dual

coaxial-cylinder Wave-Energy Converter. Appl Ocean Res, 59 (2016) 577-588.

[13] Tom N, Son D, Belissen V, Yeung RW. Modeling of a Permanent Magnet Linear Generator for Wave-Energy Conversion. ASME 2015 34th International Conference on Ocean, Offshore and Arctic Engineering: American Society of Mechanical Engineers; 2015. p. V009T009A024-V009T009A024.

[14] Eriksson M, Isberg J, Leijon M, Hydrodynamic modelling of a direct drive wave energy converter. International Journal of Engineering Science, 43 (2005) 1377-1387.

[15] Li W, Isberg J, Engström J, Waters R, Leijon M, Parametric study of the power absorption for a linear generator wave energy converter. J Ocean Wind Energy, 2 (2015) 248-252.

[16] Kimoulakis NM, Kladas AG, Tegopoulos JA, Power generation optimization from sea waves by using a permanent magnet linear generator drive. IEEE Transactions on Magnetics, 44 (2008) 1530-1533.

[17] Zheng Z-Q, Huang P, Gao D-X, Chang Z-Y, Analysis of electromagnetic force of the linear generator in point absorber wave energy converters. Journal of Marine Science and Technology, 23 (2015) 475-480.

[18] de la Villa Jaén A, Santana AG, Considering linear generator copper losses on model predictive control for a point absorber wave energy converter. Energy Conversion and management, 78 (2014) 173-183.

[19] Tom N, Yeung RW, Experimental confirmation of nonlinear-model-predictive control applied offline to a permanent magnet linear generator for ocean-wave energy conversion. IEEE Journal of Oceanic Engineering, 41 (2015) 281-295.

[20] Mavrakos SA, Hydrodynamic coefficients in heave of two concentric surface-piercing truncated circular cylinders. Applied Ocean Research, 26 (2004) 84-97.

[21] Molin B, On the piston and sloshing modes in moonpools. J Fluid Mech, 430 (2001) 27-50.

[22] Faltinsen O, Timokha A, On damping of two-dimensional piston-mode sloshing in a rectangular moonpool under forced heave motions. J Fluid Mech, 772 (2015).

[23] Kim J, Koh H, Cho I, Kim M, Kweon H, Experimental study of wave energy extraction by a dual-buoy heaving system. International Journal of Naval Architecture and Ocean Engineering, 9 (2017) 25-34.

[24] Baker N, Mueller MA. Direct drive wave energy converters. Rev Energ Ren: Power Engineering2001. p. 1-7.

[25] Fukuda K, Behavior of water in vertical well with bottom Opening of Ship, and its Effects on Ship-Motion. Journal of the Society of Naval Architects of Japan, 1977 (1977) 107-122.

[26] Koo BJ, Kim MH, Hydrodynamic interactions and relative motions of two floating platforms with mooring lines in side-by-side offloading operation. Appl Ocean Res, 27 (2005) 292-310.

[27] Ran Z. Coupled dynamic analysis of floating structures in waves and currents [Dissertation]. College Station, TX: Texas A&M University; 2000.

[28] Kang H, Kim M, Hydrodynamic interactions and coupled dynamics between a container ship and multiple mobile harbors. Ocean Systems Engineering, 2 (2012) 217-228.

[29] Lee D, Kim M. Two-Body Resonant Interactions by Fully Coupled Method and Partially Coupled Method. Civil Engineering in the Oceans VI2006. p. 494-503.

[30] Rhinefrank K, Agamloh E, von Jouanne A, Wallace A, Prudell J, Kimble K, et al., Novel ocean energy permanent magnet linear generator buoy. Renewable Energy, 31 (2006) 1279-1298.

[31] Stephen NG, On energy harvesting from ambient vibration. Journal of sound and vibration, 293 (2006) 409-425.

[32] Cho I, Kim M, Enhancement of wave-energy-conversion efficiency of a single power buoy with inner dynamic system by intentional mismatching strategy. Ocean Systems Engineering, 3 (2013) 203-217.

[33] Jensen JS, Pedersen NL, On maximal eigenfrequency separation in two-material structures: the 1D and 2D scalar cases. Journal of Sound and Vibration, 289 (2006) 967-986.